

Microstructural and compositional design principles for Mo-V-Nb-Ti-Zr multi-principal element alloys: a high-throughput first-principles study

Zhidong Leong^a, Upadrasta Ramamurty^{b,c}, Teck Leong Tan^{a,*}

^a*Institute of High Performance Computing, Agency for Science, Technology and Research, Singapore 138632, Singapore*

^b*School of Mechanical and Aerospace Engineering, Nanyang Technological University, Singapore 639798, Singapore*

^c*Institute of Materials Research and Engineering, Agency for Science, Technology and Research, Singapore 138634, Singapore*

Abstract

Due to the vast compositional space of multi-principal element alloys (MPEAs), the rational design of MPEAs for optimized microstructures is difficult. Therefore, a high-throughput first-principles study of Mo-V-Nb-Ti-Zr, a refractory MPEA, was conducted to gain insights into the underlying microstructures. Using Monte-Carlo simulations powered by cluster expansion, we uncover the principles governing the MPEA's microstructures across a large compositional space that includes non-equiatomic compositions and encompasses the constituent binaries, ternaries, and quaternaries. In the spirit of Hume-Rothery rules for complete solid solubility, we present a quantitative expression for predicting solid solution formation from the composition. Within a consistent framework, our results reproduce the microstructural observations (solid solution vs. segregation) from numerous experiments and provide microstructural predictions for unexplored regions in the compositional space. Our work illuminates the MPEA's microstructures in terms of the separation and clustering tendencies of the elements, presenting a set of simple but powerful design principles for future experiments to rationally design MPEAs with the desired microstructures for superior mechanical properties.

Keywords: Multi-principal element alloys, Microstructure design, First-principles calculations, High-entropy alloys, Refractory alloys

1. Introduction

An extension of the original design concept of high-entropy alloys (HEAs), multi-principal element alloys (MPEAs) are alloys with three or more principal components of comparable, but not necessarily equal, compositions [1]. In pursuing rational design strategies for MPEAs, the field of MPEAs focuses on stabilizing the solid-solution phase via maximizing the configurational entropy, as well as using secondary phases to optimize the strength-ductility combinations. However, the exceptional tunability of MPEAs is a double-edged sword: while it can lead to physical properties superior to those of conventional alloys [2–4], it complicates the understanding of MPEAs and hence hinders rational design.

For example, refractory MPEAs, such as Mo-V-Nb-Ti-Zr, have been studied for their high-temperature strength [5–8] and biomechanical compatibility [9–13] for aerospace and biomedical applications, respectively. However, insights into the physics of refractory MPEAs remain limited [6], because experiments are often restricted to just a small number of compositions within the huge compositional space, which has vastly expanded in MPEA design.

With additive manufacturing, there is also rising interests in compositionally graded MPEAs [14, 15] and compositionally inhomogeneous MPEAs [16]. Therefore, a general high-throughput computational methodology that covers the full compositional design space of MPEAs, including both equiatomic and non-equiatomic compositions, would be timely. Such a study can reveal insights into the thermodynamic origins of the MPEA microstructures, guiding future experiments in the rational design of MPEAs with the desired properties and microstructures.

In the study of MPEAs, information about the microstructures in relation to temperature and composition is important for design purposes because they impact mechanical properties [17–23]. In particular, understanding the formation of solid solutions vis-à-vis the precipitation of secondary phases is critical [6, 24]. While Hume-Rothery rules [25–27] are popular empirical rules for predicting solid solution formation in conventional alloys, applying these rules to MPEAs is not always reliable. Hence, the prediction of solid solution formation in MPEAs remains a key priority of active research [28–31].

Experimentally, X-ray diffraction (XRD) and various microscopy techniques are often used to resolve the microstructures of MPEAs [32, 33]. The slow diffusion kinetics in MPEAs [34] does not allow for the design of alloys with long-term microstructural stability. In this context, the thermodynamic transition temperature, T_c , is a

*Corresponding author

Email addresses: leong_zhidong@ihpc.a-star.edu.sg (Zhidong Leong), uram@ntu.edu.sg (Upadrasta Ramamurty), tantl@ihpc.a-star.edu.sg (Teck Leong Tan)

key material characteristic. Above T_c , the solid-solution phase is thermodynamically stable. Below T_c , the formation of secondary phases becomes energetically favorable [35]. Therefore, a compositional map of T_c , as well as the microstructural information on phase formation, is highly desirable.

In this work, we elucidate the compositional dependence of the microstructures of Mo-V-Nb-Ti-Zr MPEAs via a high-throughput first-principles study. Using cluster expansion (CE) within Monte Carlo (MC) simulations, we predict that, over the whole compositional design space, the single-phase solid solution at high temperatures cools into two segregated secondary phases: one Zr-rich and the other enriched with Mo and V, while Nb and Ti remain randomly dispersed. Tracing the short-range ordering within the microstructures reveals that this phase formation is predominantly driven by Zr-V segregation tendency, followed by Mo-V clustering tendency. Consequently, a higher V content accelerates secondary phase formation and increases the T_c . In the spirit of Hume-Rothery rules, we present a quantitative expression for predicting the T_c and identify compositions that preclude solid solution formation. The accuracy of our methodology is validated by the agreement with the experimental data available at various compositions and conditions [32, 36, 37]. Our work serves to guide the rational design of MPEAs with the desired microstructures and mechanical properties.

2. Methods

2.1. Cluster expansion

Cluster expansion (CE) [38] is a popular computational technique for modeling crystalline alloy properties. Based on the generalized Ising model, the formation energies of alloy structures are expanded in CE in terms of the effective cluster interactions (ECIs) of the relevant atomic clusters (see Appendix B for details). By fitting to energies calculated from first-principles, ECIs between various elemental species in the alloy can be determined. The result is a surrogate model that rapidly and accurately computes the formation energy of any alloy structure, enabling high-throughput thermodynamic studies of MPEAs.

While there exists abundant literature on using CE to study binary and ternary alloys [39–55], studies on quaternary [17, 56–58] and quinary [59, 60] alloys remain limited and are restricted to a small number of compositions. Practical applications thus far include designing AlNiCo permanent magnets [59] and radiation resistant materials [58] using MPEAs.

Here, we train our CE model of Mo-V-Nb-Ti-Zr (henceforth abbreviated as MVNTZ) using the formation energies of 10265 alloy structures based on density functional theory (DFT) (see Appendix A). Our CE is based on the bcc lattice because the solid solution phases of all the ten constituent binaries are known to have such a lattice structure. To ensure that our training data is representative,

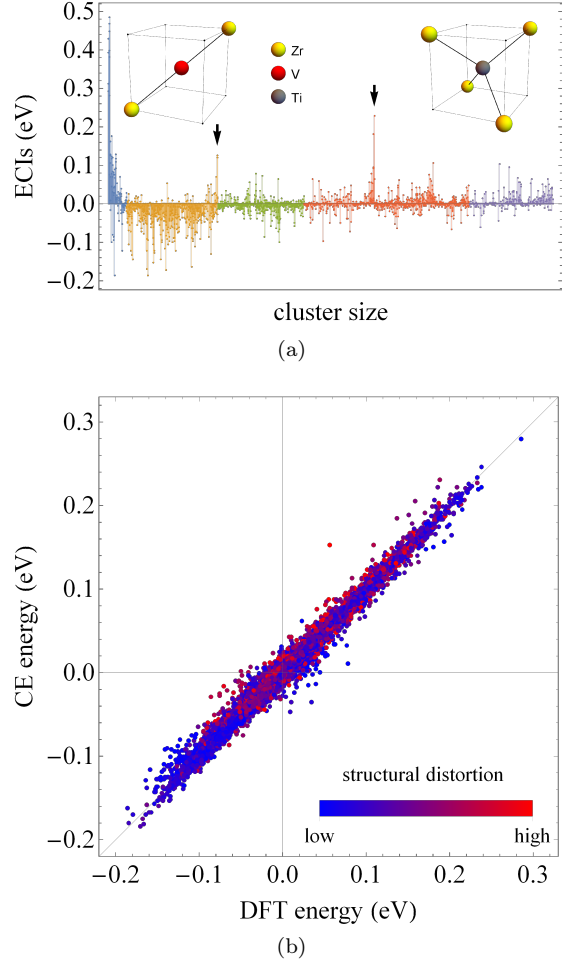


Figure 1: Cluster expansion (CE) of MVNTZ, trained with the first-principles formation energies of 10265 alloy structures. The cross-validation score is 9.2 meV. (a) The fitted values of the 2911 ECIs. Pairs, triplets, quadruplets, five-bodies, and six-bodies are colored blue, orange, green, red, and purple, respectively. Insets: the three- and five-body Zr-rich clusters corresponding to the large ECIs marked by the arrows. (b) A plot of the predicted CE energies against the DFT energies for the training structures. Each point is colored based on the degree of structural distortion.

we include binary to quinary structures covering a wide range of compositions.

A key challenge in CE involves selecting the most predictive set of atomic clusters as descriptors—an exhaustive search is computationally prohibitive due to the large number of possible combinations, particularly for MPEAs. Alloy structures with significant structural distortions (e.g. due to large atomic size mismatch [52] or high Zr content [61]) are also known to complicate cluster selection in CE. In a recent work [62], we developed an efficient physics-based learning methodology for cluster selection. Based on group lasso [63], this methodology selects a parsimonious set of atomic clusters in accordance with the physical insight that if a cluster is selected, its subclusters should be too [64]. Equivalently, a cluster’s ECI is nonzero only if the ECIs of all its subclusters are also nonzero. These selection rules avoid spuriously large fitting parameters by

redistributing them among lower-order terms, resulting in more physical, accurate, and robust CEs. A parsimonious CE consisting of just the essential ECIs is important for accelerating the sampling of the MPEA’s configurational space during subsequent MC simulations. In this present paper, we apply group lasso to study MPEAs.

Fig. 1a shows the fitted values of the ECIs. From an initial pool of 2911 atomic clusters consisting of two- to six-body clusters, group lasso has selected 75% of them for the CE; the ECIs of the remaining 25% have been set to zero to yield a parsimonious model. The fitted ECIs exhibit good convergence—the magnitude of the ECIs generally decreases with increasing cluster size. The spikes among some of the triplets and larger clusters are necessary for capturing the effects of structural distortion, particularly in Zr-rich structures (see Fig. D.2b). As the insets highlight, these clusters tend to have high Zr content. Indeed, Fig. D.3 shows that these spikes vanish if we were to train our CE model with the undistorted structures instead, i.e., structures where only the unit cell parameters are relaxed (no local relaxation of atomic positions). Accurately modeling the effects of structural distortions in MVNTZ using higher-order interactions is important for the quantitative agreement between CE predictions and DFT energies. Shown in Fig. 1b and further detailed in Fig. D.2a, this agreement is quantified by a cross-validation score of 9.2 meV and is good even for structures with high degrees of distortion. This accurate surrogate model of MVNTZ is the key machinery that enables the high-throughput MC simulations in this work, for producing thermodynamics and microstructural information across compositions.

2.2. Monte Carlo (MC) simulations

We perform MC simulations at 505 compositions, where the concentration of each elemental species has values 0, 0.1, 0.2, 0.3, 0.4, 0.5 with a nonzero amount of Zr. These compositions span a space large enough to include almost all reasonable definitions of MPEAs. Our canonical MC simulations are based on the Metropolis algorithm as implemented in our Thermodynamic Toolkit (TTK) [35, 49]. Each simulation contains $24 \times 24 \times 24$ atoms within the periodic simulation box, using 500 equilibrium steps and 2000 sampling steps. These values are fixed and are deemed sufficient for convergence by benchmarking our results for the constituent binary systems against known phase diagrams. At each composition, the simulation begins in the solid solution phase at a sufficiently high temperature and cools with a temperature step of $\Delta T = 10$ meV ~ 116 K, for a total of 37 temperatures.

2.3. Short-range order (SRO) parameters

The microstructures observed in MC simulations can be characterized by using the Warren-Cowley short-range order (SRO) parameters [65] to track the elemental distributions. In our work, we focus on the nearest-neighbor (NN) SRO parameter. For elemental species $i \neq j$, the NN SRO parameter is given by

$$\alpha_{ij} = 1 - \frac{p_{ij}}{c_i c_j}, \quad (1)$$

where c_i, c_j are the concentrations of species i, j , and p_{ij} is the probability of a NN atomic pair having species i, j in the first and second sites, respectively. It follows that $\alpha = 0$ indicates a fully random arrangement, $0 < \alpha \leq 1$ a segregation tendency, and $\alpha < 0$ a tendency for the species to cluster.

3. Results

3.1. Clustering/segregation tendency

We begin with the MC simulations of MVNTZ at equi-composition. Fig. 2a illustrates the SROs of the observed microstructures. As the high-temperature quinary solid solution cools, Zr most notably segregates from Mo and V, while Mo and V tend to cluster. In both phases, Nb and Ti remain randomly dispersed. We determine a transition temperature of $T_c \sim 1850$ K based on the cusps of the Zr SROs (see Appendix E for details). As the temperature decreases further, Zr segregation becomes more pronounced and V also segregates from Nb and Ti, while complex intermetallics involving all five elemental species begin forming.

These observations are represented in Fig. 2b-2d, which provide snapshots of the microstructures at three representative temperatures. Each snapshot is accompanied by a graphical representation of the SROs, where the vertices represent the five elemental species and the ten edges are colored based on the SROs’ values—a darker pink (green) edge indicates a higher segregation (clustering) tendency.

A thermodynamic description of the microstructural evolution can thus be summarized as such: Well above the T_c at 2900 K, all five elements are randomly dispersed in a single-phase solid solution. At 1400 K, which is slightly below the T_c , there are two segregated secondary phases: one Zr-rich and the other a disordered phase enriched with Mo and V, which possess a small clustering tendency. The remaining elements Nb and Ti are distributed rather evenly between the two phases. These observations are consistent with experimental measurements of samples annealed at 1673 K [32], except for a third (non-bcc) Laves phase which is naturally beyond the scope of our bcc simulations. Our simulations further predict that, way below the T_c at 600 K (probably experimentally inaccessible due to MPEAs’ sluggish dynamics), there is further segregation to at least three intermetallic phases, such as Mo-V, Mo-Ti, and Nb-Zr.

3.2. Extension to the multidimensional compositional space

While experiments are restricted to a small number compositions, the computational efficiency of CE enables a high-throughput study of the MPEAs’ multidimensional compositional space. Here, we extend our MC simulations and SRO characterization to a total of 505 compositions,

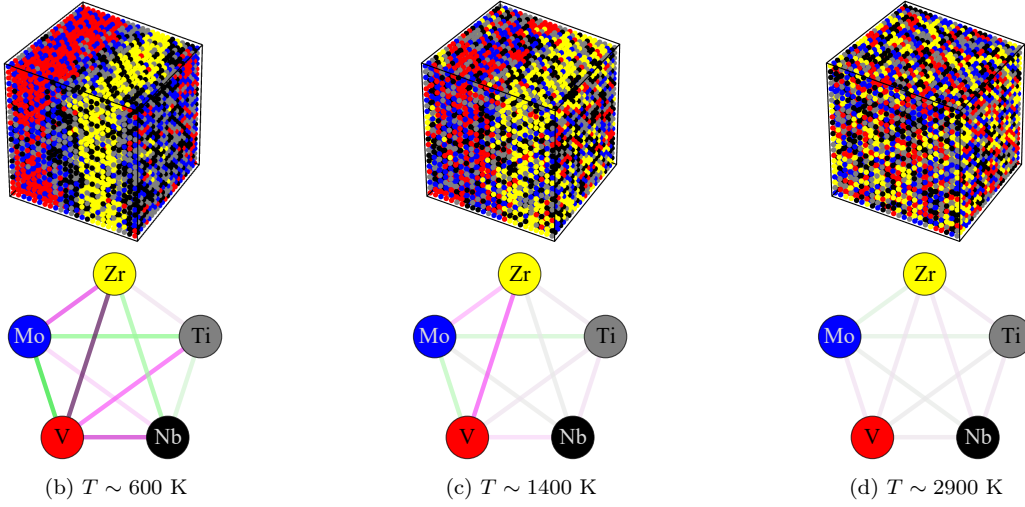
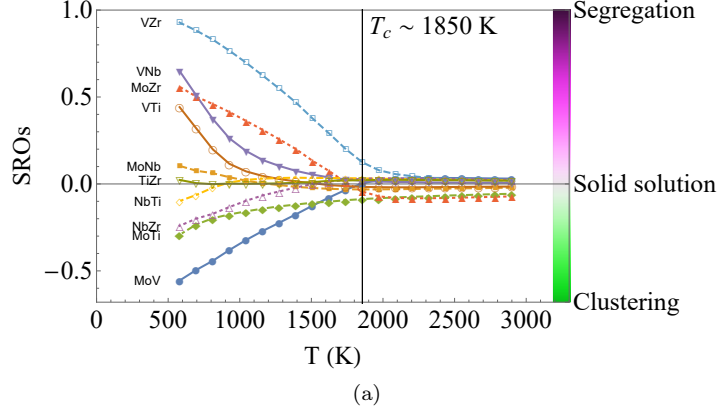


Figure 2: The microstructures of equicompositional MoVNbTiZr. (a) The temperature dependence of the ten short-range orders characterizing the microstructures. As the solid solution cools, Zr segregates from Mo and V, while Mo and V tend to cluster. Nb and Ti are generally evenly dispersed throughout the system. (b-d) Snapshots of the microstructures at three representative temperatures. Each microstructure is characterized by a graphical representation of the SROs, where the vertices represent the five elements and the edges are colored based on the SROs' values, according to the bar legend in (a).

spread across the whole compositional space relevant to MPEAs.

Across all compositions, Zr-Mo and Zr-V segregation were observed as predominant. As expected, T_c is highly composition-dependent, which is modeled using a simple-to-use quadratic polynomial. With respect to the concentrations, $\mathbf{x} = (x_{\text{Mo}} \ x_{\text{V}} \ x_{\text{Nb}} \ x_{\text{Ti}})^T$:

$$T_c / (1.16 \times 10^4 \text{ K}) = -0.25 + \begin{pmatrix} 1.3 \\ 1.8 \\ 1.0 \\ 0.7 \end{pmatrix} \mathbf{x} - \mathbf{x}^T \begin{pmatrix} 1.1 & 0.9 & 0.8 & 0.6 \\ 0.9 & 1.3 & 1.1 & 1.0 \\ 0.8 & 1.1 & 0.7 & 0.6 \\ 0.6 & 1.0 & 0.6 & 0.4 \end{pmatrix} \mathbf{x}, \quad (2)$$

where the coefficient matrix has been symmetrized. The rms error of the fit is about 128 K, similar to the temperature step size in the MC simulations. Detailed in Fig. F.1, the equation is most reliable for $T_c \gtrsim 1400$ K, a temperature range which includes typical annealing temperatures in experiments. Furthermore, fitting smooths

out numerical uncertainties from the MC simulations (e.g. due to potentially insufficient MC sampling). Most importantly, this fit enables rapid compositional design by predicting solid solution formation across the wide concentration ranges of MPEAs.

3.3. Validation from the experimental data

First, we focus on $\text{Mo}_x\text{V}_y\text{NbTiZr}$, where experimental data are available to benchmark our predictions. For as-cast samples [36, 37], $\text{Mo}_x\text{V}_y\text{NbTiZr}$ is a single-phase solid solution when either the Mo- or V-content is low. When $x > 1$ and $y = 1$, the MPEA segregates into a Mo-rich, Zr-deficient dendritic phase with Zr-rich precipitates that are deficient in Mo and Nb. When $y = 1$ and $x \geq 1.5$, we similarly have Zr segregation. For samples annealed at 1673 K [32], NbTiZr is a single-phase solid solution while VNbTiZr consists of V-rich precipitates surrounded by Zr-rich regions. The microstructure of quinary MoVNbTiZr is more complex: it consists of Zr-deficient dendrites surrounded by interdendritic regions rich in Zr and Ti but deficient in Mo and V, as well as a $(\text{Mo}, \text{V})_2\text{Zr}$ C15 Laves phase.

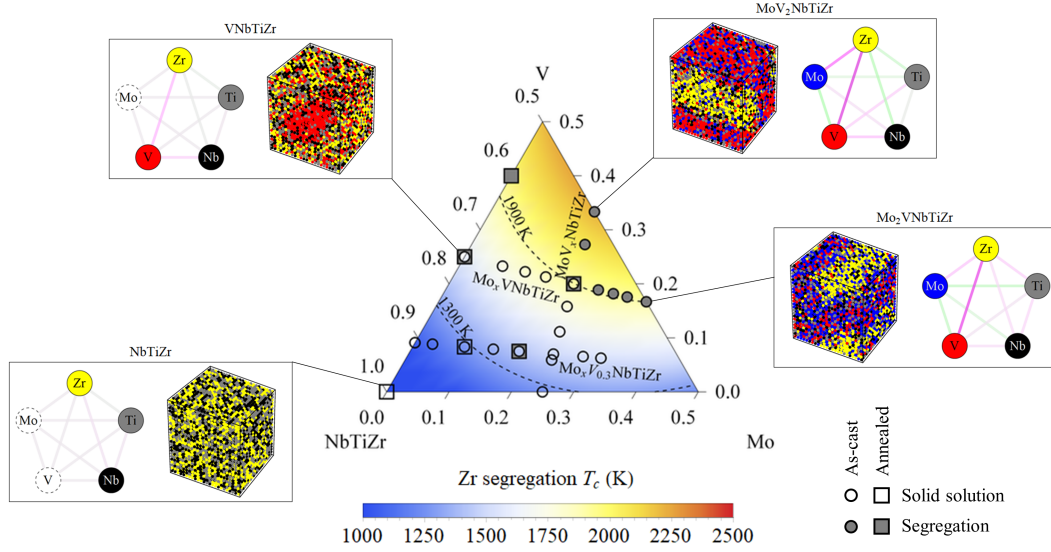


Figure 3: Experimental validation of $\text{Mo}_x\text{V}_y(\text{NbTiZr})_{1-x-y}$ microstructures for $0 \leq x + y \leq 0.5$. A ternary plot of the T_c from first-principles is overlaid with existing experimental data based on as-cast [36, 37] and annealed [32, 37, 66, 67] samples. Circles (squares) indicate compositions studied using as-cast (annealed) samples. An unfilled (filled) symbol represents the observation of a solid solution (segregated phase). The contour lines at 1900 K (1300 K) guide the eye at dividing single phases from multiphases for as-cast (annealed) samples. Both first-principles and experimental observations agree that higher concentrations of Mo and V promote phase segregation. The microstructures at four representative compositions are shown for $T^* \sim 1400$ K. Each microstructure is accompanied by a graphical representation of the SROs, where the vertices represent the five species and the edges are colored based on values of the SROs—a darker pink (green) edge indicates a stronger tendency to segregate (cluster).

Similarly, samples of VNbTiZr and V_2NbTiZr annealed at 1473 K contain V-rich, Zr-deficient regions and Zr-rich, V-deficient regions [66, 67]. Finally, for samples annealed at 1273 K [37], $\text{Mo}_{0.3}\text{V}_{0.3}\text{NbTiZr}$ remains as a single-phase solid solution, but $\text{Mo}_{0.7}\text{V}_{0.3}\text{NbTiZr}$ segregates into two bcc phases and a C15 Laves phase.

We summarize in Fig. 3 these experimental observations of Zr segregation. Across compositions, the segregation is strongly affected by Mo and V content. Among samples of the same type (as-cast or annealed), phase segregation occurs at higher concentrations of Mo and V.

To compare with the experimental findings, we overlay our first-principles-derived T_c in the form of a contour plot using Eq. 2, where a lower T_c implies a higher tendency for the formation of a single solid-solution phase. As shown in Fig. 3, the predicted T_c increases with the concentration of V, in support of experimental findings. This dependence can be traced back to Eq. 2, where the linear term in V-concentration is the largest contribution. The agreement with experiments is accentuated by the observation that contour lines of the T_c neatly demarcate the solid-solution samples from the phase-segregated samples, i.e., the solid-solution (phase-segregated) samples lie in the bluer (redder) regions of the contour plot.

Fig. 3 also showcases our MC-simulated microstructures of a few representative systems at $T^* \sim 1400$ K, which is close to the experimental annealing temperatures (1273–1673 K) in Ref. [32, 37, 66, 67]. For compositions with $T_c > T^*$, the SRO reflect the segregation of Zr from Mo and V, similar to that at equicomposition. Across dif-

ferent compositions, segregation is more pronounced for higher T_c .

Fig. 4 presents the analogous T_c ternary plots where the concentrations of other pairs of elements are varied: $\text{Mo}_x\text{VNb}_y\text{TiZr}$, $\text{Mo}_x\text{VNbTi}_y\text{Zr}$, $\text{MoV}_x\text{Nb}_y\text{TiZr}$, $\text{MoV}_x\text{NbTi}_y\text{Zr}$, and $\text{MoVNb}_x\text{Ti}_y\text{Zr}$, for $0 \leq x + y \leq 0.5$. In these cases, the Zr content is deliberately substantial because of its role in the phase segregations.

Unlike $\text{Mo}_x\text{V}_y\text{NbTiZr}$ in Fig. 3, there exist limited experimental studies of the microstructures for these compositions [68]. Therefore, our computational results here are predictions of the MVNTZ microstructures in the unexplored regions of the compositional space: MVNTZ phase segregates similarly to Fig. 3, with the T_c given by Fig. 4 and Eq. 2. This knowledge of the temperature and compositional dependence of the microstructure can be used to tune the mechanical properties of the MPEAs using different thermal histories [69], through various strengthening mechanisms [24].

A lower T_c implies a more stable solid solution phase. Hence, the bluer regions in Fig. 4 illustrate the compositions for which a (single-phase) solid solution is more likely to be found. This is true provided that the predicted T_c is less than T_m , the melting temperature. Therefore, we have also indicated in Fig. 4 the compositions for which $T_c > T_m$ (see Appendix C). Note that for $\text{Mo}_x\text{V}_y\text{NbTiZr}$ in Fig. 3, $T_c < T_m$ at all points in the ternary diagram.

Taking into account practical considerations, we propose three specific compositions for future experimental studies. Based on the MC simulations, each of these sys-

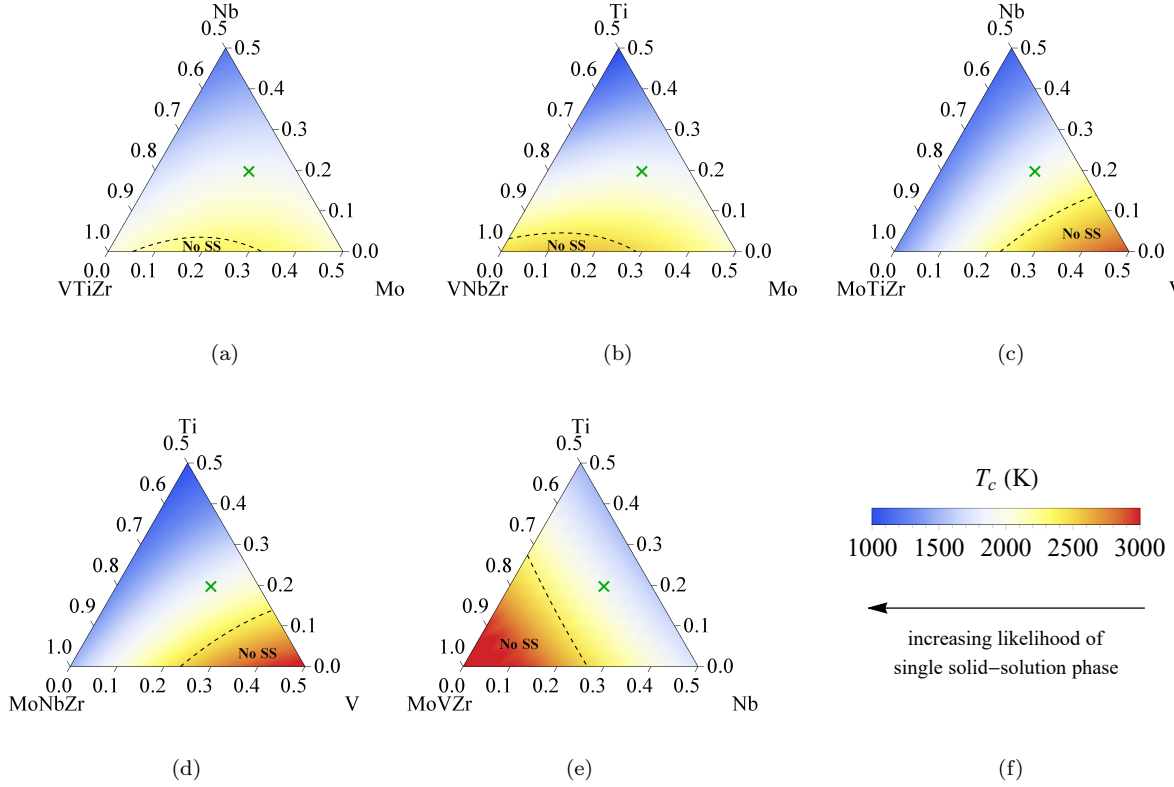


Figure 4: Stability of the solid solution phase in MVNTZ across compositions. Ternary plots of the T_c for (a) $\text{Mo}_x\text{VNb}_y\text{TiZr}$, (b) $\text{Mo}_x\text{VNbTi}_y\text{Zr}$, (c) $\text{MoV}_x\text{Nb}_y\text{TiZr}$, (d) $\text{MoV}_x\text{NbTi}_y\text{Zr}$, and (e) $\text{MoVNb}_x\text{Ti}_y\text{Zr}$, for $0 \leq x + y \leq 0.5$, with the legend given in (f). In each plot, the dashed line is given by $T_c = T_m$, the melting temperature. When $T_c > T_m$, a solid solution phase is prohibited. The green cross in each plot indicates equicomposition.

tems is a single-phase solid solution at 1400 K, which is around the typical annealing temperature. By favoring Ti over Mo, the MPEA VNbTi_2Zr is a solid solution with reduced density ($\rho \sim 6.08 \text{ g cm}^{-3}$ based on the rule of mixtures). Such an MPEA could be useful as lightweight alloys in the aerospace industry [66, 70]. Among the five elemental species, Ti has the lowest density ($\rho_{\text{Ti}} = 4.51 \text{ g cm}^{-3}$) while Mo has the highest ($\rho_{\text{Mo}} = 10.3 \text{ g cm}^{-3}$). By omitting V, the MPEAs MoNbTi_2Zr and MoNb_2TiZr are solid solutions with improved biocompatibility, as V ions are known to exhibit cytotoxicity [71, 72]. Such MPEAs could be useful as biomedical implants.

3.4. Origin of phase segregation

While Zr segregates from Mo and V throughout the compositional space, one may wonder what happens when either Mo or V is absent from it. Here, we illustrate the microstructures of two such cases (Fig. 5), compared with that at equicomposition (Fig. 2c).

Without Mo, the quaternary system in Fig. 5a is best described as V segregated. While Zr-V segregation remains predominant, Nb and Ti are now concentrated in the Zr-rich phase. This shows that Nb and Ti prefer clustering with Zr over V, forming a V-rich phase and a phase rich in Zr, Nb, and Ti. Experimentally, samples of VNbTiZr

and V_2NbTiZr annealed at 1473 K phase segregates into Zr-rich and V-rich bcc phases [66]. Compression deformation at 1273 K of the V_2NbTiZr samples induces a more complete transformation such that the V-rich phase also becomes Ti-deficient [70]. These observations are consistent with the results from MC simulations.

Without V, Fig 5b shows that Zr now segregates from Nb and Ti, while Mo is evenly distributed. Zr-Mo segregation is noticeably suppressed, suggesting that Zr-Mo segregation at equicomposition is driven by the combination of Zr-V segregation and Mo-V clustering tendency. Furthermore, we observe that that Nb and Ti prefer clustering with Mo over Zr. This suggests that, at equicomposition, Nb and Ti has a tendency to cluster with Mo but segregate from V. This tendency competes against the Mo-V clustering tendency, suppressing the segregation of V from Nb and Ti. This suppression is well illustrated by comparing Figs. 5a and 5c, which contains Mo instead of Zr. In this case, we also observe that, without Zr, the T_c is low ($< 1000 \text{ K}$), confirming Zr's role in the predominant behavior of MVNTZ at equicomposition. This is consistent with the observation of a solid solution in as-cast MoVNbTi [20].

To summarize, we provide four key principles governing the thermodynamics of MVNTZ MPEAs:

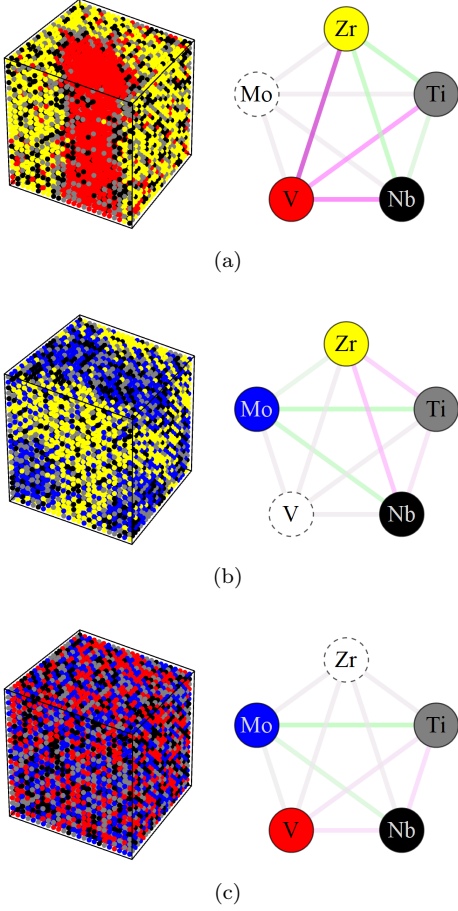


Figure 5: Three quaternary edge cases. The microstructures and SROs of (a) $V_3Nb_2Ti_2Zr_3$, (b) $Mo_3Nb_2Ti_2Zr_3$, and (c) $Mo_3V_3Nb_2Ti_2$ at 1000 K. In the graphical representations of the SROs, the vertices represent the five species and the edges are colored based on values of the SROs—a darker pink (green) edge indicates a stronger tendency to segregate (cluster). The vertices of excluded elements are shown in white with dashed borders.

- (1): V-Zr segregation is the predominant behavior.
- (2): Mo and V tend to cluster. This and (1) together promote Mo-Zr segregation.
- (3): Nb and Ti have a hierarchical clustering tendency, preferring Mo over Zr, and Zr over V.
- (4): The competition between (2) and (3) moderates the tendency for V-Nb and V-Ti segregation and Mo-V clustering.

In general, the precise behaviors at any composition is a fine balance between the tendency for certain elemental species to cluster or segregate. These principles help elucidate the origin of phase segregation in the quinary system, providing a deeper understanding of the microstructural behaviors of MPEAs.

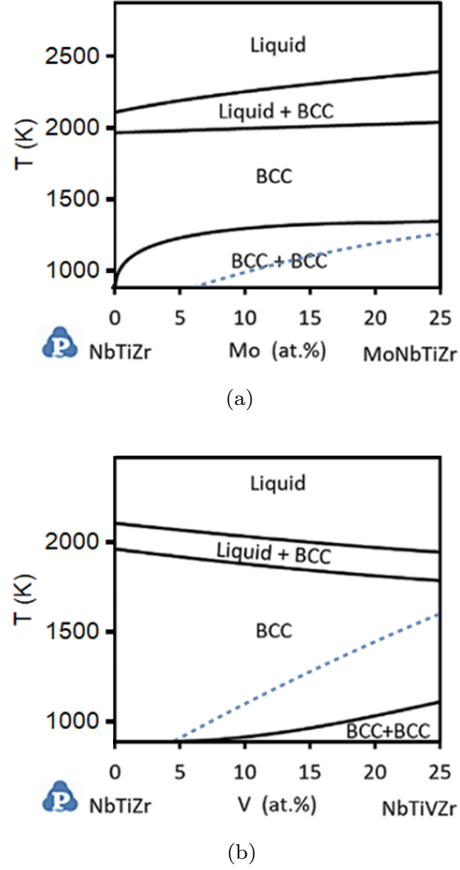


Figure 6: A comparison of the CALPHAD phase diagrams (solid lines) from Ref. [73] with our CE-based T_c (dashed lines), for (a) $Mo_x(NbTiZr)_{1-x}$ and (b) $V_x(NbTiZr)_{1-x}$.

4. Discussion

In Fig. 6, we compare our T_c from Eq. 2 with the results based on CALPHAD from Ref. [73]. Both sets of results are consistent for practical purposes—experiments are unlikely to favor one set of computational results over the other given the slow kinetics in the MPEA, especially at lower temperatures. This is true except for $VNbTiZr$, where CALPHAD predicts a much lower T_c (~ 1100 K) than our first-principles-derived results (~ 1600 K). Existing experimental data shows that $VNbTiZr$ phase segregates even for samples annealed between 1473–1673 K [32, 66, 67], contradicting the low T_c that CALPHAD predicts. As noted in Ref. [1, 73], reliable CALPHAD results for MPEAs require a complete thermodynamic database—extrapolations from incomplete data of the constituent binary/ternary alloys could produce incorrect results. Predicting the phases of MPEAs using CALPHAD remains an active field of research [31, 74]. In contrast, our model goes beyond the extrapolation of binary or ternary data, since the first-principles training data for our model include quaternary and quinary structures as well. The importance of these higher order contributions is further highlighted by the sizable ECIs (shown in Fig. 1a) for clusters containing four or more different elemental species. Therefore,

this comparison for VNbTiZr showcases an example in which the MC-derived T_c , built upon first-principles data computed over all relevant MPEA compositions (from binary to quinary), is more consistent with experiments than CALPHAD is.

In Fig. 4, we identified regions within the composition space for which solid solution formation is prohibited. The accuracy of these regions undoubtedly depends on the T_m estimates used. In fact, a more accurate treatment would involve the temperature range over which solidification takes place. Doing so would enlarge, in Fig. 4, the bounded regions that prohibit solid solution formation.

Our DFT and MC calculations are based on a bcc lattice because each of the five elements of MVNTZ forms a bcc lattice in the solid solution phase. This is true even for Ti and Zr, which form hcp structures at low temperatures. Furthermore, existing experimental data of MVNTZ also show a predominant bcc phase [32, 36, 37, 66, 67]. However, given the limited understanding of MPEAs, phases with other lattice structures, such as the Laves phase, could also exist. Reproducing such phases is possible in principle, with separate sets of DFT and MC calculations for different lattices.

5. Conclusions

We have presented a high-throughput first-principles study of refractory MPEA Mo-V-Nb-Ti-Zr. Based on the formation energies of a set of highly representative structures, we constructed a cluster expansion model that enables high-throughput Monte Carlo simulations. Across the entire compositional design space, we predicted that the high-temperature solid solution cools into two segregated secondary phases: one Zr-rich and the other enriched with Mo and V, while Nb and Ti remain evenly distributed. By characterizing the microstructures using short-range order, we identify the predominant driving force to be Zr-V segregation, which together with the clustering tendency of Mo and V, also leads to Mo-Zr segregation. Quantitatively, we encapsulated the results of our high-throughput study in a practical expression for predicting the T_c from the composition. We showed that the T_c , and hence the tendency for phase segregation, most significantly increases with V content, and we identified compositions for which solid solution formation is prohibited. Within a consistent framework, our results reproduce the phases observed in numerous sets of experiments from literature. Our results provide the highly desired insights into the MPEA’s microstructures, guiding future experiments towards the appropriate regions within the composition space when designing MPEAs with superior mechanical properties.

Acknowledgments

The authors thank the Advanced Manufacturing and Engineering Young Individual Research Grant (AME YIRG)

of Agency for Science, Technology and Research (A*STAR) (A1884c0016) for financial support. The DFT computations in this article were performed on the resources of the National Supercomputing Centre, Singapore (<https://www.nsc.sg>).

Appendix A. DFT calculations

The energies of the CE training structures are calculated based on density functional theory (DFT) with the Vienna Ab initio Simulation Package (VASP) [75, 76]. We use the Perdew, Burke, and Ernzerhof exchange correlation based on the generalized gradient approximation [77, 78]. The projector augmented-wave potentials are used with the outer p semicore states included in the valence states [79, 80]. Planewave cutoffs are set to 520 eV. For each structure, two sets of constrained relaxation are performed. In the initial relaxation, only the cell volume is relaxed, keeping the atom positions and cell shape fixed to that of a bcc lattice (ISIF = 7). From this semi-relaxed structure, we further relaxed the atomic positions (ISIF = 2); this results in structures with cubic unit cells but with atom positions shifted from their ideal bcc positions. The resulting structures are thus representative of MPEAs/HEAs at moderate to high temperatures, where the overall structure is observed to have a cubic symmetry but with the possibility of local lattice distortions. The energy reduction during the second stage of relaxation gives the structural distortion energy that quantifies the degree of distortion in Fig. 1b. Our convergence criterion is based on keeping the Hellmann-Feynman force on each atom below 0.015 eV/Å. Calculations are not spin polarized as Mo, Nb, V, Ti, and Zr are not known to be strongly magnetic. The k -point mesh is generated using a Γ grid and density of 200 Å⁻³.

Appendix B. Cluster expansion

Based on the generalized Ising model, CE expands the configurational energy $E(\sigma)$ of an alloy structure, σ , in terms of atomic clusters α , where the cluster correlation functions $\Phi_\alpha(\sigma)$ serve as the basis set and the effective cluster interactions (ECIs) V_α serve as the coefficients:

$$E(\sigma) = \sum_{\alpha} \Phi_{\alpha}(\sigma) V_{\alpha}. \quad (\text{B.1})$$

By fitting to first-principles energies, the ECIs between various elemental species in the alloy can be determined.

The 10265 training structures of the CE are selected from a pool of derivative structures, systematically generated up to a six-atom unit cell [81, 82]. Shown in Fig. D.1, the structures contain between two to five elemental species. Our CE-derived models are therefore built upon data spread across a large compositional space, including up to quinary data. This is unlike CALPHAD, whose model are based on binary or ternary data only.

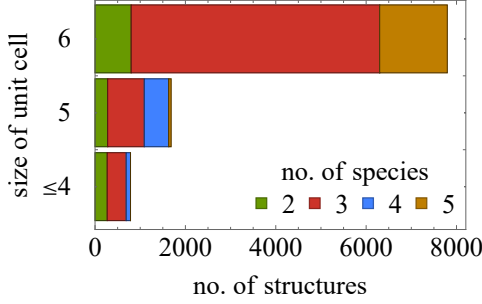


Figure D.1: Among the 10265 derivative structures used for training the CE models, the bar chart shows the distribution of unit cell sizes and the number of elemental species.

In our CE, we treat V, Nb, Ti, and Zr as the independent species, while Mo is treated as dependent. As such, only clusters formed by V, Nb, Ti, and Zr atoms are required. In the bcc lattice, we consider up to the 12th-nearest-neighbor (12NN) pairs, 5NN triplets, and 3NN four-body to six-body clusters. These correspond to an initial pool of 2911 symmetrically distinct clusters, consisting of 120 pairs, 596 triplets, 565 four-body clusters, 1080 five-body clusters, and 550 six-body clusters.

Our fitting procedure follows our earlier work in Ref. [62]. Using the DFT formation energies of the training structures, we use group lasso to select a properly truncated CE set from the initial 2911 distinct clusters. Five-fold cross-validation is used for selecting the optimal hyperparameter with the one-standard-error rule. In the trained CE, 2175 out of the initial 2911 clusters are selected.

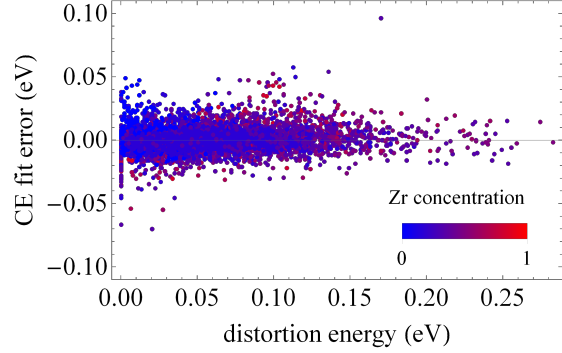
Appendix C. Melting temperature

The melting temperature T_m in Fig. 4 is approximated by the simple weighted average of the compositions: $T_m = \sum_i x_i T_{m,i}$, where the elemental melting temperatures in ascending order are $T_{m,Ti} = 1941$ K, $T_{m,Zr} = 2128$ K, $T_{m,V} = 2183$ K, $T_{m,Nb} = 2750$ K, and $T_{m,Mo} = 2896$ K.

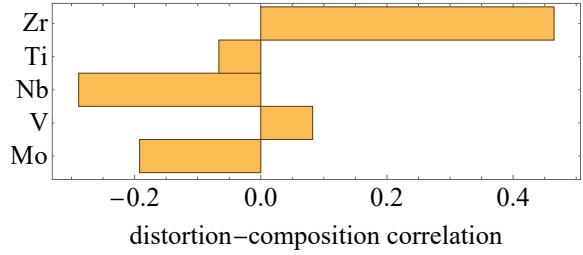
Appendix D. Structural distortion in cluster expansion

For the 10265 derivative structures detailed in Figure D.1, we quantify the degree of structural distortion in DFT by the distortion energy. Figure D.2a shows that our CE fit is accurate even for structures with large distortions, implying that the CE has captured the effects of distortion. Also, we observe that structures with higher Zr content tends to have larger distortion. We quantify this by calculating the correlation (Pearson correlation coefficient) between the distortion energy and the concentration of each elements. Figure D.2b shows that Zr, among the five elements, contributes most to distortion.

To elucidate the effects of structural distortion, we train another CE model with structures without distortion, where the atomic positions are unrelaxed and remain



(a)



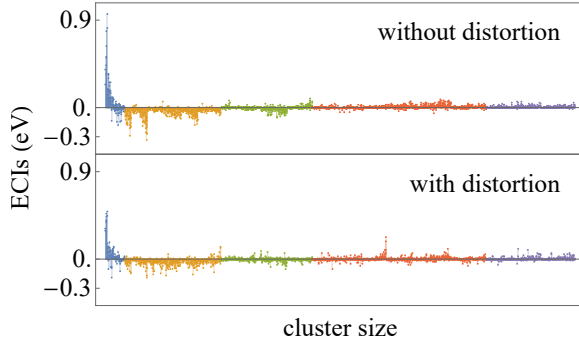
(b)

Figure D.2: (a) A plot of the CE fitting error against the distortion energy for the 10265 training structures. Bluer (Redder) points correspond to structures with lower (higher) Zr content. (b) The correlation between distortion energy and concentration of each of the five elements. Here, correlation ranges from -1 to 1. Structures with higher Zr content tend to have more structural distortion.

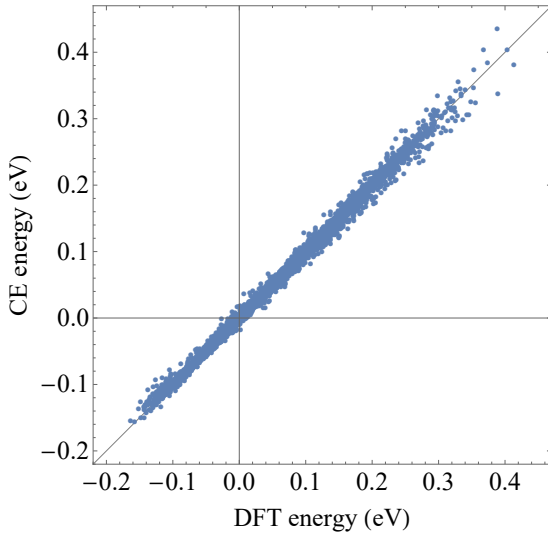
in their original ideal bcc lattice positions. Figure D.3a compares the resulting ECIs of CEs with and without distortion. Without distortion, ECIs are well behaved and without large fluctuations in higher-order ECIs (triplets and beyond). The effects of distortion are captured by shifting contributions from pair ECIs to the ECIs of the relevant higher-order clusters. Finally, Figure D.3b shows that without distortion, the CV score is 5.4 meV. With distortion, the slightly higher CV score quantifies the extent CE captures the effects of distortion: CE captures distortion partially, but well.

Appendix E. Computing the T_c

The T_c 's are computed from the cusps of the SROs of Zr with respect to all the other elements. Zr SROs are used because Zr segregation is the predominant behavior in the system. As the solid solution phase cools, Zr is the first species to undergo a transition, as indicated by the cusps in the SROs. For any elemental pair, the SRO's cusp is defined as the temperature at which the magnitude of the SRO's second derivative is maximum: $T_{\text{cusp}} = \text{argmax}_T |d^2 \text{SRO} / dT^2|$, with the derivatives computed using finite differences. Among these SROs, the highest-temperature cusp determines the T_c .



(a)



(b)

Figure D.3: (a) Comparing the two sets of 2911 ECIs from CEs based on structures (bottom) with and (top) without structural distortion. Pairs, triplets, quadruplets, five-bodies, and six-bodies are colored blue, orange, green, red, and purple, respectively. (b) A plot of the predicted CE energies against the DFT energies for the training structures without distortion. The cross-validation score is 5.4 meV.

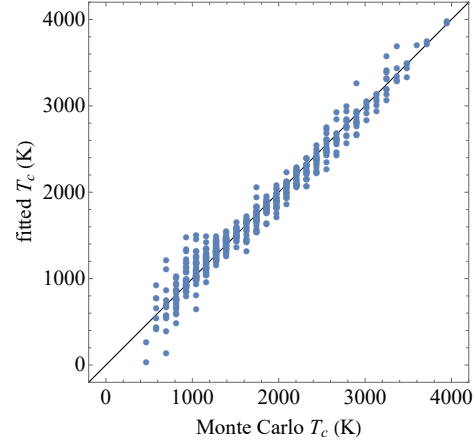


Figure F.1: A plot of the fitted T_c against the T_c from MC simulations at 505 compositions.

Appendix F. Fitting the T_c

Figure F.1 compares the fitted T_c with the T_c from the MC simulations at 505 compositions. The rms error of the fit is 128 K, comparable to the temperature step size in the MC simulations. The fit is noticeably better at higher temperatures $T \gtrsim 1400$ K, which include all the temperatures of interest in the main text. Fitting the T_c to a higher order polynomial does not substantially improve the accuracy of the fit. A more accuracy fit would require a more complex functional form containing thermodynamic considerations.

References

- [1] D. B. Miracle, High entropy alloys as a bold step forward in alloy development, *Nature Communications* 10 (2019) 1805. doi:10.1038/s41467-019-09700-1.
- [2] E. P. George, D. Raabe, R. O. Ritchie, High-entropy alloys, *Nature Reviews Materials* 4 (2019) 515–534. doi:10.1038/s41578-019-0121-4.
- [3] D. B. Miracle, O. N. Senkov, A critical review of high entropy alloys and related concepts, *Acta Materialia* 122 (2017) 448–511. doi:10.1016/j.actamat.2016.08.081.
- [4] Y. Zhao, D.-H. Lee, M.-Y. Seok, J.-A. Lee, M. P. Phaniraj, J.-Y. Suh, H.-Y. Ha, J.-Y. Kim, U. Ramamurty, J.-i. Jang, Resistance of CoCrFeMnNi high-entropy alloy to gaseous hydrogen embrittlement, *Scripta Materialia* 135 (2017) 54–58. doi:10.1016/j.scriptamat.2017.03.029.
- [5] O. Senkov, S. Rao, T. Butler, T. Daboiku, K. Chaput, Microstructure and properties of Nb-Mo-Zr based refractory alloys, *International Journal of Refractory Metals and Hard Materials* 92 (2020) 105321. doi:10.1016/j.ijrmhm.2020.105321.
- [6] O. N. Senkov, D. B. Miracle, K. J. Chaput, J.-P. Couzinie, Development and exploration of refractory high entropy alloys—A review, *Journal of Materials Research* 33 (2018) 3092–3128. doi:10.1557/jmr.2018.153.
- [7] O. N. Senkov, G. B. Wilks, D. B. Miracle, C. P. Chuang, P. K. Liaw, Refractory high-entropy alloys, *Intermetallics* 18 (2010) 1758–1765. doi:10.1016/j.intermet.2010.05.014.
- [8] C.-C. Juan, M.-H. Tsai, C.-W. Tsai, C.-M. Lin, W.-R. Wang, C.-C. Yang, S.-K. Chen, S.-J. Lin, J.-W. Yeh, Enhanced mechanical properties of HfMoTaTiZr and HfMoNbTaTiZr re-

- fractory high-entropy alloys, *Intermetallics* 62 (2015) 76–83. doi:10.1016/j.intermet.2015.03.013.
- [9] P. Chui, R. Jing, F. Zhang, J. Li, T. Feng, Mechanical properties and corrosion behavior of β -type Ti-Zr-Nb-Mo alloys for biomedical application, *Journal of Alloys and Compounds* 842 (2020) 155693. doi:10.1016/j.jallcom.2020.155693.
 - [10] W.-Y. Ching, S. San, J. Brechtel, R. Sakidja, M. Zhang, P. K. Liaw, Fundamental electronic structure and multiautomic bonding in 13 biocompatible high-entropy alloys, *npj Computational Materials* 6 (2020) 1–10. doi:10.1038/s41524-020-0321-x.
 - [11] Y. Yuan, Y. Wu, Z. Yang, X. Liang, Z. Lei, H. Huang, H. Wang, X. Liu, K. An, W. Wu, Z. Lu, Formation, structure and properties of biocompatible TiZrHfNbTa high-entropy alloys, *Materials Research Letters* 7 (2019) 225–231. doi:10.1080/21663831.2019.1584592.
 - [12] M. Todai, T. Nagase, T. Hori, A. Matsugaki, A. Sekita, T. Nakano, Novel TiNbTaZrMo high-entropy alloys for metallic biomaterials, *Scripta Materialia* 129 (2017) 65–68. doi:10.1016/j.scriptamat.2016.10.028.
 - [13] T. Nagase, Y. Iijima, A. Matsugaki, K. Ameyama, T. Nakano, Design and fabrication of Ti–Zr–Hf–Cr–Mo and Ti–Zr–Hf–Co–Cr–Mo high-entropy alloys as metallic biomaterials, *Materials Science and Engineering: C* 107 (2020) 110322. doi:10.1016/j.msec.2019.110322.
 - [14] H. Döbelstein, E. L. Gurevich, E. P. George, A. Ostendorf, G. Laplanche, Laser metal deposition of compositionally graded TiZrNbTa refractory high-entropy alloys using elemental powder blends, *Additive Manufacturing* 25 (2019) 252–262. doi:10.1016/j.addma.2018.10.042.
 - [15] B. Gwalani, S. Gangireddy, S. Shukla, C. J. Yannetta, S. G. Valentin, R. S. Mishra, R. Banerjee, Compositionally graded high entropy alloy with a strong front and ductile back, *Materials Today Communications* 20 (2019) 100602. doi:10.1016/j.mtcomm.2019.100602.
 - [16] R. Chang, W. Fang, H. Yu, X. Bai, X. Zhang, B. Liu, F. Yin, Heterogeneous banded precipitation of (CoCrNi)₉₃Mo₇ medium entropy alloys towards strength–ductility synergy utilizing compositional inhomogeneity, *Scripta Materialia* 172 (2019) 144–148. doi:10.1016/j.scriptamat.2019.07.026.
 - [17] R. Feng, P. K. Liaw, M. C. Gao, M. Widom, First-principles prediction of high-entropy-alloy stability, *npj Computational Materials* 3 (2017). doi:10.1038/s41524-017-0049-4.
 - [18] J. Ding, Q. Yu, M. Asta, R. O. Ritchie, Tunable stacking fault energies by tailoring local chemical order in CrCoNi medium-entropy alloys, *Proceedings of the National Academy of Sciences* 115 (2018) 8919–8924. doi:10.1073/pnas.1808660115.
 - [19] X.-G. Li, C. Chen, H. Zheng, Y. Zuo, S. P. Ong, Complex strengthening mechanisms in the NbMoTaW multi-principal element alloy, *npj Computational Materials* 6 (2020) 1–10. doi:10.1038/s41524-020-0339-0.
 - [20] S. Y. Chen, X. Yang, K. A. Dahmen, P. K. Liaw, Y. Zhang, Microstructures and Crackling Noise of AlxNbTiMoV High Entropy Alloys, *Entropy* 16 (2014) 870–884. doi:10.3390/e16020870.
 - [21] C. Varvenne, G. Leyson, M. Ghazisaeidi, W. Curtin, Solute strengthening in random alloys, *Acta Materialia* 124 (2017) 660–683. doi:10.1016/j.actamat.2016.09.046.
 - [22] P. Kumar, U. Ramamurty, Microstructural optimization through heat treatment for enhancing the fracture toughness and fatigue crack growth resistance of selective laser melted Ti6Al4V alloy, *Acta Materialia* 169 (2019) 45–59. doi:10.1016/j.actamat.2019.03.003.
 - [23] Y. Zhao, X. Wang, T. Cao, J.-K. Han, M. Kawasaki, J.-i. Jang, H. N. Han, U. Ramamurty, L. Wang, Y. Xue, Effect of grain size on the strain rate sensitivity of CoCrFeNi high-entropy alloy, *Materials Science and Engineering: A* 782 (2020) 139281. doi:10.1016/j.msea.2020.139281.
 - [24] I. Basu, J. T. M. De Hosson, Strengthening mechanisms in high entropy alloys: Fundamental issues, *Scripta Materialia* 187 (2020) 148–156. doi:10.1016/j.scriptamat.2020.06.019.
 - [25] W. Hume-Rothery, H. M. Powell, On the theory of super-lattice structures in alloys, *Zeitschrift für Kristallographie-Crystalline Materials* 91 (1935) 23–47.
 - [26] W. Hume-Rothery, *Atomic Theory for Students of Metallurgy*, Inst. Metals Mono. Rep., Institute of Metals, London, 1952.
 - [27] W. Hume-Rothery, C. W. Haworth, R. E. Smallman, *The Structure of Metals and Alloys*, fifth ed., Institute of Metals and the Institution of Metallurgists, London, 1969.
 - [28] O. N. Senkov, J. D. Miller, D. B. Miracle, C. Woodward, Accelerated exploration of multi-principal element alloys with solid solution phases, *Nature Communications* 6 (2015) 1–10. doi:10.1038/ncomms7529.
 - [29] J.-H. Li, M.-H. Tsai, Theories for predicting simple solid solution high-entropy alloys: Classification, accuracy, and important factors impacting accuracy, *Scripta Materialia* 188 (2020) 80–87. doi:10.1016/j.scriptamat.2020.06.064.
 - [30] Z. Pei, J. Yin, J. A. Hawk, D. E. Alman, M. C. Gao, Machine-learning informed prediction of high-entropy solid solution formation: Beyond the Hume-Rothery rules, *npj Computational Materials* 6 (2020) 1–8. doi:10.1038/s41524-020-0308-7.
 - [31] Y. Zeng, M. Man, K. Bai, Y.-W. Zhang, Revealing high-fidelity phase selection rules for high entropy alloys: A combined CALPHAD and machine learning study, *Materials & Design* 202 (2021) 109532. doi:10.1016/j.matdes.2021.109532.
 - [32] O. N. Senkov, S. Rao, K. J. Chaput, C. Woodward, Compositional effect on microstructure and properties of NbTiZr-based complex concentrated alloys, *Acta Materialia* 151 (2018) 201–215. doi:10.1016/j.actamat.2018.03.065.
 - [33] K. G. Pradeep, Atomic-scale compositional characterization of a nanocrystalline AlCrCuFeNiZn high-entropy alloy using atom probe tomography, *Acta Materialia* (2013) 11.
 - [34] M.-H. Tsai, J.-W. Yeh, High-Entropy Alloys: A Critical Review, *Materials Research Letters* 2 (2014) 107–123. doi:10.1080/21663831.2014.912690.
 - [35] N. A. Zarkevich, T. L. Tan, D. D. Johnson, First-principles prediction of phase-segregating alloy phase diagrams and a rapid design estimate of their transition temperatures, *Physical Review B* 75 (2007) 104203. doi:10.1103/PhysRevB.75.104203.
 - [36] Y. Zhang, X. Yang, P. K. Liaw, Alloy Design and Properties Optimization of High-Entropy Alloys, *JOM* 64 (2012) 830–838. doi:10.1007/s11837-012-0366-5.
 - [37] Y. Wu, Y. Cai, X. Chen, T. Wang, J. Si, L. Wang, Y. Wang, X. Hui, Phase composition and solid solution strengthening effect in TiZrNbMoV high-entropy alloys, *Materials & Design* 83 (2015) 651–660. doi:10.1016/j.matdes.2015.06.072.
 - [38] J. Sanchez, F. Ducastelle, D. Gratias, Generalized cluster description of multicomponent systems, *Physica A: Statistical Mechanics and its Applications* 128 (1984) 334–350. doi:10.1016/0378-4371(84)90096-7.
 - [39] J. W. D. Connolly, A. R. Williams, Density-functional theory applied to phase transformations in transition-metal alloys, *Physical Review B* 27 (1983) 5169–5172. doi:10.1103/PhysRevB.27.5169.
 - [40] Z. W. Lu, S.-H. Wei, A. Zunger, Long-range order in binary late-transition-metal alloys, *Physical Review Letters* 66 (1991) 1753–1756. doi:10.1103/PhysRevLett.66.1753.
 - [41] C. Wolverton, G. Ceder, D. de Fontaine, H. Dreyse, Ab initio ground-state study with fourth-nearest-neighbor cluster interactions for fcc Pd-V alloys, *Physical Review B* 45 (1992) 13105–13108. doi:10.1103/PhysRevB.45.13105.
 - [42] G. D. Garbulsky, G. Ceder, Effect of lattice vibrations on the ordering tendencies in substitutional binary alloys, *Physical Review B* 49 (1994) 6327–6330. doi:10.1103/PhysRevB.49.6327.
 - [43] V. Ozoliņš, C. Wolverton, A. Zunger, Cu-Au, Ag-Au, Cu-Ag, and Ni-Au intermetallics: First-principles study of temperature-composition phase diagrams and structures, *Physical Review B* 57 (1998) 6427–6443. doi:10.1103/PhysRevB.57.6427.
 - [44] S. Müller, A. Zunger, First-Principles Predictions of Yet-Unobserved Ordered Structures in the Ag-Pd Phase Diagram, *Physical Review Letters* 87 (2001) 165502. doi:10.1103/PhysRevLett.87.165502.
 - [45] A. Zunger, L. G. Wang, G. L. W. Hart, M. Sanati, Obtain-

- ing Ising-like expansions for binary alloys from first principles, *Modelling and Simulation in Materials Science and Engineering* 10 (2002) 685.
- [46] A. van de Walle, M. Asta, First-principles investigation of perfect and diffuse antiphase boundaries in HCP-based Ti-Al alloys, *Metallurgical and Materials Transactions A* 33 (2002) 735–741. doi:10.1007/s11661-002-0139-9.
 - [47] V. Blum, A. Zunger, Structural complexity in binary bcc ground states: The case of bcc Mo-Ta, *Physical Review B* 69 (2004). doi:10.1103/PhysRevB.69.020103.
 - [48] G. L. W. Hart, V. Blum, M. J. Walorski, A. Zunger, Evolutionary approach for determining first-principles hamiltonians, *Nature Materials* 4 (2005) 391–394. doi:10.1038/nmat1374.
 - [49] N. A. Zarkevich, T. L. Tan, L.-L. Wang, D. D. Johnson, Low-energy antiphase boundaries, degenerate superstructures, and phase stability in frustrated fcc Ising model and Ag-Au alloys, *Physical Review B* 77 (2008). doi:10.1103/PhysRevB.77.144208.
 - [50] A. van de Walle, Multicomponent multisublattice alloys, non-configurational entropy and other additions to the Alloy Theoretic Automated Toolkit, *Calphad* 33 (2009) 266–278. doi:10.1016/j.calphad.2008.12.005.
 - [51] T. L. Tan, L.-L. Wang, D. D. Johnson, K. Bai, A Comprehensive Search for Stable Pt-Pd Nanoalloy Configurations and Their Use as Tunable Catalysts, *Nano Letters* 12 (2012) 4875–4880. doi:10.1021/nl302405k.
 - [52] C. Ravi, B. K. Panigrahi, M. C. Valsakumar, A. van de Walle, First-principles calculation of phase equilibrium of V-Nb, V-Ta, and Nb-Ta alloys, *Physical Review B* 85 (2012) 054202. doi:10.1103/PhysRevB.85.054202.
 - [53] L. J. Nelson, G. L. W. Hart, F. Zhou, V. Ozoliņš, Compressive sensing as a paradigm for building physics models, *Physical Review B* 87 (2013). doi:10.1103/PhysRevB.87.035125.
 - [54] J. S. Wróbel, D. Nguyen-Manh, M. Y. Lavrentiev, M. Muzyk, S. L. Dudarev, Phase stability of ternary fcc and bcc Fe-Cr-Ni alloys, *Physical Review B* 91 (2015). doi:10.1103/PhysRevB.91.024108.
 - [55] A. Van der Ven, J. Thomas, B. Puchala, A. Natarajan, First-Principles Statistical Mechanics of Multicomponent Crystals, *Annual Review of Materials Research* 48 (2018) 27–55. doi:10.1146/annurev-matsci-070317-124443.
 - [56] S. B. Maisel, M. Höfler, S. Müller, Configurationally exhaustive first-principles study of a quaternary superalloy with a vast configuration space, *Physical Review B* 94 (2016). doi:10.1103/PhysRevB.94.014116.
 - [57] A. Fernández-Caballero, M. Fedorov, J. S. Wróbel, P. M. Mummery, D. Nguyen-Manh, Configurational Entropy in Multicomponent Alloys: Matrix Formulation from Ab Initio Based Hamiltonian and Application to the FCC Cr-Fe-Mn-Ni System, *Entropy* 21 (2019) 68. doi:10.3390/e21010068.
 - [58] O. El-Atwani, N. Li, M. Li, A. Devaraj, J. K. S. Baldwin, M. M. Schneider, D. Sobieraj, J. S. Wróbel, D. Nguyen-Manh, S. A. Maloy, E. Martinez, Outstanding radiation resistance of tungsten-based high-entropy alloys, *Science Advances* 5 (2019) eaav2002. doi:10.1126/sciadv.aav2002.
 - [59] M. C. Nguyen, L. Zhou, W. Tang, M. J. Kramer, I. E. Anderson, C.-Z. Wang, K.-M. Ho, Cluster-Expansion Model for Complex Quinary Alloys: Application to Alnico Permanent Magnets, *Physical Review Applied* 8 (2017). doi:10.1103/PhysRevApplied.8.054016.
 - [60] A. Fernández-Caballero, J. S. Wróbel, P. M. Mummery, D. Nguyen-Manh, Short-Range Order in High Entropy Alloys: Theoretical Formulation and Application to Mo-Nb-Ta-V-W System, *Journal of Phase Equilibria and Diffusion* 38 (2017) 391–403. doi:10.1007/s11669-017-0582-3.
 - [61] Y. Tong, S. Zhao, H. Bei, T. Egami, Y. Zhang, F. Zhang, Severe local lattice distortion in Zr- and/or Hf-containing refractory multi-principal element alloys, *Acta Materialia* 183 (2020) 172–181. doi:10.1016/j.actamat.2019.11.026.
 - [62] Z. Leong, T. L. Tan, Robust cluster expansion of multicomponent systems using structured sparsity, *Physical Review B* 100 (2019) 134108. doi:10.1103/PhysRevB.100.134108.
 - [63] M. Yuan, Y. Lin, Model selection and estimation in regression with grouped variables, *Journal of the Royal Statistical Society: Series B (Statistical Methodology)* 68 (2006) 49–67. doi:10.1111/j.1467-9868.2005.00532.x.
 - [64] N. A. Zarkevich, D. D. Johnson, Reliable First-Principles Alloy Thermodynamics via Truncated Cluster Expansions, *Physical Review Letters* 92 (2004). doi:10.1103/PhysRevLett.92.255702.
 - [65] D. D. Fontaine, The number of independent pair-correlation functions in multicomponent systems, *Journal of Applied Crystallography* 4 (1971) 15–19. doi:10.1107/S0021889871006174.
 - [66] O. N. Senkov, S. V. Senkova, C. Woodward, D. B. Miracle, Low-density, refractory multi-principal element alloys of the Cr-Nb-Ti-V-Zr system: Microstructure and phase analysis, *Acta Materialia* 61 (2013) 1545–1557. doi:10.1016/j.actamat.2012.11.032.
 - [67] T. Butler, K. Chaput, J. Dietrich, O. Senkov, High temperature oxidation behaviors of equimolar NbTiZrV and NbTiZrCr refractory complex concentrated alloys (RCCAs), *Journal of Alloys and Compounds* 729 (2017) 1004–1019. doi:10.1016/j.jallcom.2017.09.164.
 - [68] Y. Mu, H. Liu, Y. Liu, X. Zhang, Y. Jiang, T. Dong, An ab initio and experimental studies of the structure, mechanical parameters and state density on the refractory high-entropy alloy systems, *Journal of Alloys and Compounds* 714 (2017) 668–680. doi:10.1016/j.jallcom.2017.04.237.
 - [69] F. He, Z. Wang, Y. Li, Q. Wu, J. Li, J. Wang, C. T. Liu, Kinetic ways of tailoring phases in high entropy alloys, *Scientific Reports* 6 (2016) 34628. doi:10.1038/srep34628.
 - [70] O. N. Senkov, S. V. Senkova, D. B. Miracle, C. Woodward, Mechanical properties of low-density, refractory multi-principal element alloys of the Cr-Nb-Ti-V-Zr system, *Materials Science and Engineering: A* 565 (2013) 51–62. doi:10.1016/j.msea.2012.12.018.
 - [71] Y. Okazaki, S. Rao, Y. Ito, T. Tateishi, Corrosion resistance, mechanical properties, corrosion fatigue strength and cytocompatibility of new Ti alloys without Al and V, *Biomaterials* 19 (1998) 1197–1215. doi:10.1016/S0142-9612(97)00235-4.
 - [72] M. F. López, J. A. Jiménez, A. Gutiérrez, Corrosion study of surface-modified vanadium-free titanium alloys, *Electrochimica Acta* 48 (2003) 1395–1401. doi:10.1016/S0013-4686(03)00006-9.
 - [73] O. N. Senkov, C. Zhang, A. L. Pilchak, E. J. Payton, C. Woodward, F. Zhang, CALPHAD-aided development of quaternary multi-principal element refractory alloys based on NbTiZr, *Journal of Alloys and Compounds* 783 (2019) 729–742. doi:10.1016/j.jallcom.2018.12.325.
 - [74] R. Li, L. Xie, W. Y. Wang, P. K. Liaw, Y. Zhang, High-Throughput Calculations for High-Entropy Alloys: A Brief Review, *Frontiers in Materials* 7 (2020). doi:10.3389/fmats.2020.00290.
 - [75] G. Kresse, J. Furthmüller, Efficiency of ab-initio total energy calculations for metals and semiconductors using a plane-wave basis set, *Computational Materials Science* 6 (1996) 15–50. doi:10.1016/0927-0256(96)00008-0.
 - [76] G. Kresse, J. Furthmüller, Efficient iterative schemes for ab initio total-energy calculations using a plane-wave basis set, *Physical Review B* 54 (1996) 11169–11186. doi:10.1103/PhysRevB.54.11169.
 - [77] J. P. Perdew, K. Burke, M. Ernzerhof, Generalized Gradient Approximation Made Simple, *Physical Review Letters* 77 (1996) 3865–3868. doi:10.1103/PhysRevLett.77.3865.
 - [78] J. P. Perdew, K. Burke, M. Ernzerhof, Generalized Gradient Approximation Made Simple [Phys. Rev. Lett. 77, 3865 (1996)], *Physical Review Letters* 78 (1997) 1396–1396. doi:10.1103/PhysRevLett.78.1396.
 - [79] P. E. Blöchl, Projector augmented-wave method, *Physical Review B* 50 (1994) 17953–17979. doi:10.1103/PhysRevB.50.17953.
 - [80] G. Kresse, D. Joubert, From ultrasoft pseudopotentials to

- the projector augmented-wave method, *Physical Review B* 59 (1999) 1758–1775. doi:10.1103/PhysRevB.59.1758.
- [81] G. L. W. Hart, R. W. Forcade, Algorithm for generating derivative structures, *Physical Review B* 77 (2008). doi:10.1103/PhysRevB.77.224115.
- [82] G. L. Hart, L. J. Nelson, R. W. Forcade, Generating derivative structures at a fixed concentration, *Computational Materials Science* 59 (2012) 101–107. doi:10.1016/j.commatsci.2012.02.015.